

Rapid detection of cracks in the rail foot by ultrasonic B-scan imaging using a shear horizontal guided wave electromagnetic acoustic transducer

Songtao Hu^a, Wenzhe Shi^{a,b}, Chao Lu^{a,c*}, Yao Chen^a, Guo Chen^a, Gongtian Shen^a

^a Key Laboratory of Nondestructive Testing, Ministry of Education, Nanchang Hangkong University, Nanchang, 330063, China

^b State Key Laboratory of Acoustics, Institute of Acoustics, Chinese Academy of Sciences, Beijing, 100190, China

^c Key Laboratory of Simulation and Numerical Modeling Technology of Jiangxi Province, Gannan Normal University, Ganzhou, 341000, China



ARTICLE INFO

Keywords:

Rail foot
Guided wave EMAT
Finite element method
Synchrosqueezed wavelet transform
Ultrasonic B-Scan imaging

ABSTRACT

Transverse cracks in the rail foot are responsible for the breaking of the rail. The existing non-destructive testing technology for high-speed railway track is difficult to perform in-situ and rapid detection for the rail foot, which poses a hidden danger to driving safety. In this study, a new method is proposed for the in-situ and rapid detection of cracks in the rail foot by ultrasonic B-scan imaging. A finite element method (FEM) based on the Bloch–Floquet boundary and domain constraint were employed to calculate the dispersion curves of shear horizontal (SH)-like guided waves propagating in the rail foot. SH guided waves mainly vibrate with in-plane displacement, and they are less affected by the rail components such as elastic clips and pads. Based on the calculated dispersion curves, an SH-guided wave electromagnetic acoustic transducer (EMAT) with a center frequency of 0.154 MHz was developed, and ultrasonic B-scan imaging was performed to detect straight cracks in the rail foot. Besides, the synchrosqueezed wavelet transform (SWT) method was proposed to remove noises and higher-order guided wave modes from the original ultrasonically detected signals. Results show that FEM with the Bloch–Floquet boundary and domain constraint can be used to solve the dispersion curves of the SH-like guided waves of the rail foot accurately and easily. The application of SWT can increase the lift-off of the EMAT, eliminate the noise, remove the higher-order SH-like guided wave modes, improve the detection efficiency, and enhance the quality of ultrasonic B-scan images. After the SWT processing, the signal-to-noise ratio (SNR) of the ultrasonic signal is increased by at least 5.98 dB. When the lift-off of the EMAT is 4 mm and without synchronous averaging, the on-line and rapid ultrasonic B-scan imaging of the rail foot using guided wave EMAT can still achieve a reasonable SNR.

1. Introduction

Transverse cracks in the rail foot are responsible for derailments and accidents [1], and early detection of these cracks can prevent enormous casualties and significant economic losses. Based on the natural wave-guide of the rail, Loveday [2] developed an ultrasonic guided wave system to monitor the integrity of railway tracks. At present, most of the studies on rail crack detection are focused on the rail head and web. However, the structural integrity of the rail foot is difficult to examine and maintain; this is the main reason for derailment. Utilizing the long-distance propagation characteristics of ultrasonic guided waves in the rail [3], the cracks in the rail foot can be rapidly detected by the acoustic transducer installed on the rail flaw detection car.

Due to the presence of local corrosion and elastic rail fastening on the

rail foot, its rapid scanning cannot be realized by a contact piezoelectric ultrasound transducer, and the intensity of Lamb guided wave will attenuation quickly along the length-direction. Therefore, the non-contact electromagnetic acoustic transducers (EMATs) have received widespread attention. Rose et al. [4] evaluated the rail flaw detection ability of Lamb wave and SH-guided wave EMATs, and the experimental results proved the high application potential of the SH-guided wave EMAT in rail crack detection. Edwards et al. [5] developed a new dual probe consisting of an EMAT and pulsed eddy current sensors, and this dual probe could improve the crack detection efficiency when compared with the traditional testing method using two non-destructive testing techniques. Petcher et al. [6] demonstrated that when an EMAT probe was mounted on a train to scan a rail and the distance between the magnet and coil was 10 mm, the EMAT still had a high defect detection

* Corresponding author. Key Laboratory of Nondestructive Testing, Ministry of Education, Nanchang Hangkong University, Nanchang, 330063, China.

E-mail addresses: luchaoniat@163.com, luchao@gnnu.edu.cn (C. Lu).

ability. In recent years, guided wave focusing inspection techniques can greatly improve the detection accuracy and sensitivity [7]. Li et al. [8] derived a simple equation to compute the 1st natural focal distance of non-axisymmetric guided waves. Sun et al. [9] proposed a new oblique point-focusing SH-guided wave EMAT configuration. The ultrasonic guided wave focusing method has been mostly and successful applied to the inspection of plates [10,11].

The propagation of guided waves is not only restricted by the dimensions of the structure, but also affected by the excitation frequency. Guided wave dispersion curves are an important basis for selecting guided wave modes. Because the rail foot has a wedge-shaped waveguide, the dispersion characteristics of this waveguide cannot be analytically calculated; thus, the dispersion curves of those special structures can only be solved by a finite element method (FEM) or a semi-analytical FEM (SAFEM) [12]. Hesse et al. [13] calculated the dispersion curves of the dominant surface wave modes for rail cross-sections using an axis-symmetric FEM model. However, the calculation of this FEM is complicated, and the guided wave mode analysis cannot be conducted at high frequencies [14]. Gavrić [15] used the SAFEM to calculate the dispersion curves of propagative waves in a free rail for the first time. Hayashi et al. [16–18] solved the dispersion curves of the rail in the frequency range of 0–100 kHz based on the SAFEM. Furthermore, according to the vibration direction of the particle in the rail foot, three typical vibrations of the rail foot were found: longitudinal, vertical, and horizontal vibration. There are a large number of propagation modes with similar phase velocities in each vibration direction. The guided waves propagating in the rail foot are complex and variable; thus, it is difficult to calculate the guided wave modes in the rail foot by the SAFEM.

Compared with the SAFEM, periodic FEM only requires the mesh of one repetitive cell, which substantially reduces the computational cost. Treyssède [19,20] analyzed elastic wave propagation in a helical waveguide by a three-dimensional FEM based on periodic boundary conditions and translation-invariant mapping. Hakoda et al. [21] calculated the dispersion curves of various uniform waveguides using the periodicity inherent to the Floquet boundary conditions.

When the rail foot is inspected by a guided wave EMAT, the obtained guided wave signals are multimodal and have poor signal-to-noise ratios (SNRs); this leads to difficulties in signal interpretation. Therefore, post-processing of these multimodal signals obtained during the monitoring of the rail foot by the EMAT is required. Because guided waves are non-stationary and transient, time-frequency representations are used for the analysis of guided wave signals. Daubechies et al. [22] proposed a new time-frequency analysis tool, called synchrosqueezed wavelet transform (SWT), which has high time-frequency resolution and reversibility. Herrera et al. [23] compared the application effects of continuous wavelet transform (CWT), complete ensemble empirical mode decomposition (CEEMD) and SWT in seismic signals. SWT possesses significantly less frequency tailing, and CEEMD is about 13 times slower than SWT. SWT has recently been used in climate research [24], structural damage detection [25], and medical signal analysis [26]. Su et al. [27] proposed a technique for identifying damage location in composite plates in an environment with strong noises by SWT processing. Bause et al. [28] introduced the SWT for the decomposition of guided wave signals and estimation of group delay. Liu et al. [29] presented an SWT-based mode separation and reconstruction method to extract individual modes from dispersive multimodal guided waves.

In this study, a method based on ultrasonic B-scan imaging and an SH-guided wave EMAT is proposed for the rapid detection of cracks in the rail foot. The inspection method consists of three steps. In step 1, a FEM model with the Bloch–Floquet boundary is used to calculate the dispersion curves of the rail foot. In step 2, the SWT is employed to remove strong noises and higher-order guided wave modes from the detected signals. In step 3, ultrasonic B-scan images are constructed by the SWT-processed signals, and cracks in the rail foot are directly identified. This work provides a noncontact guided wave technique for

the rapid detection of cracks in the rail foot using an SH-guided wave EMAT with a large lift-off.

2. Principles and methods

2.1. Solution method for dispersion curves

The finite element vibration equation of an elastomer can be established by D'Alembert's principle, and the corresponding motion equation is [30].

$$M\ddot{u} + C\dot{u} + Ku = f \quad (1)$$

where M , C , K , f , and u , \dot{u} , and \ddot{u} are the structural mass matrix, viscous damping matrix, structural stiffness matrix, vector of the applied loads, displacement vector and its first- and second-order derivatives, respectively.

When eigenfrequency is solved, the finite element is in a state of undamped free vibration, that is $C = f = 0$. The displacement equation is $u = Ue^{i\omega t}$, where U , ω , t are the displacement vector matrix, angular frequency, time, respectively. Then, Equation (1) can be simplified as [31].

$$[K - \omega^2 M]U = 0 \quad (2)$$

The elastomer can be discretized into unit cells, as shown in Fig. 1. According to Floquet–Bloch theory, the unit cell displacement fields of the source surface and target surface can be written as [32].

$$U_{dst} = U_{src} e^{ikl} \quad (3)$$

where U_{src} and U_{dst} are the displacement fields of the source and target surfaces, respectively, l is the cell length of the source and target displacement fields, and k is the wave vector.

An infinite plate was discretized into unit cells, as shown in Fig. 1. Floquet periodic boundary conditions were applied in the x - and y -directions of the unit cell model, whereas free boundary condition was applied in the z -direction of the unit cell model. Consequently, this model was periodically extended in the x - and y -directions to represent an infinite-plate waveguide, which greatly reduced the computational difficulties. In the range of k , a commercial finite element software was used to solve the eigenfrequency corresponding to each k .

2.2. Configuration of periodic-permanent-magnet electromagnetic acoustic transducer (PPM-EMAT)

Fig. 2 shows the configuration of the PPM-EMAT. The dominant conversion mechanism of the PPM-EMAT is based on the generation of Lorentz forces. The EMAT coil wire runs in the direction of the alternating magnetic field, and when the current is passed through the coil, eddy currents are created in the ferromagnetic metal. Lorentz forces and magnetostriction generated by this periodic permanent magnet (PPM) EMAT generate a shearing force at the surface of the sample, with the Lorentz force being the dominant mechanism in the generation of ultrasound waves within the sample [33,34]. Because the magnetostriction mechanism to SH wave generation propagating in the desired direction is negligible, thus this EMAT configuration is referred to as a Lorentz-force EMAT [33].

Under a periodic magnetic field, Lorentz forces are generated parallel to the metal surface and perpendicular to the wire direction. The alternating Lorentz forces produce periodic vibrations that generate ultrasonic waves in the ferromagnetic metal, and the wavelength of the SH-guided waves is twice the width of the magnet [35]. The Lorentz forces f_l can be calculated by Refs. [36,37].

$$f_l = J_e \times (B_s + B_d) \quad (4)$$

where J_e is the eddy current density, B_s and B_d are the static and dynamic

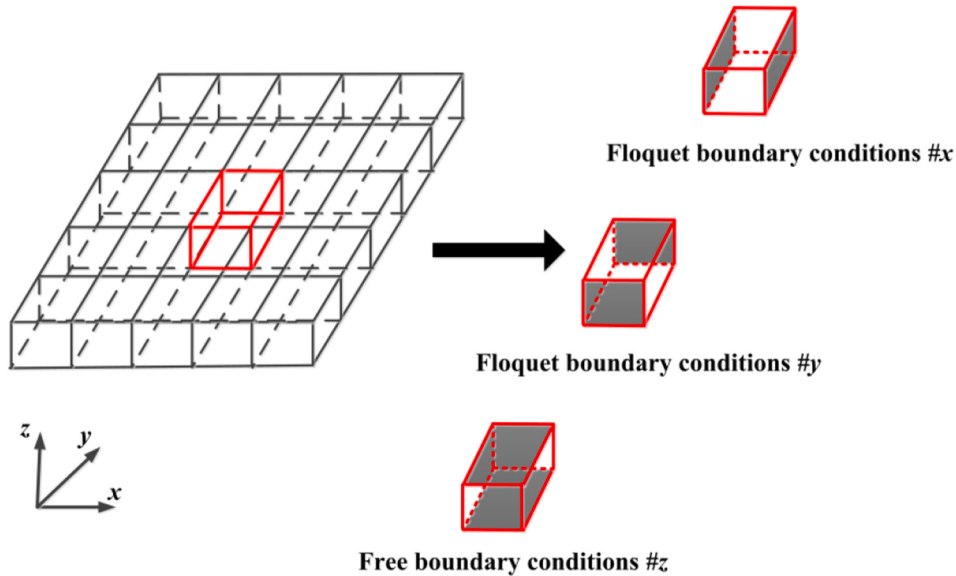


Fig. 1. Unit cell and boundary definition of the finite element model for calculating the dispersion curves.

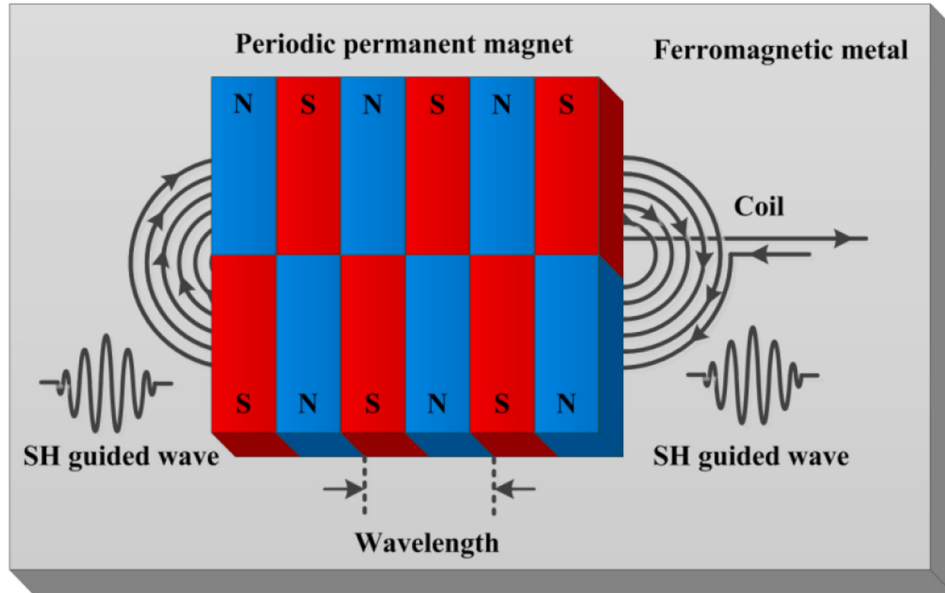


Fig. 2. Configuration of a PPM-EMAT for generating and receiving SH-guided waves.

magnetic flux density.

2.3. Principle of the SWT

CWT of the signal $f(t)$ is defined as [38].

$$W_f(a, b) = \frac{1}{\sqrt{a}} \int_{-\infty}^{+\infty} f(t) \Psi^* \left(\frac{t-b}{a} \right) dt \quad (5)$$

where a , b , and Ψ^* are the scale, time offset, and complex conjugate of the mother wavelet, respectively.

The instantaneous frequency can be estimated by the derivatives of the wavelet coefficients [25].

$$\omega_f(a, b) = \begin{cases} -j\partial_b W_f(a, b), & W_f(a, b) \neq 0 \\ \infty, & W_f(a, b) = 0 \end{cases} \quad (6)$$

The energy was transferred from the time-scale plane (b, a) to the time-frequency plane $[b, \omega_f(a, b)]$, which was then rearranged to focus the energy. When a , b , and ω were discretized, $a_s - a_{s-1} = (\Delta a)_s$. The SWT $T_f(\omega_l, b)$ was determined at the centres ω_l of the frequency range

$$\left[\omega_l - \frac{1}{2}\Delta\omega, \omega_l + \frac{1}{2}\Delta\omega \right],$$

$$T_f(\omega_l, b) = \sum_{a_s: |\omega_f(a, b) - \omega_l| \leq \frac{\Delta\omega}{2}} W_f(a, b) a_s^{-\frac{1}{2}} (\Delta a)_s \quad (7)$$

where a_s is the discrete scale, and s is the number of scales.

Each component of the original signal $h(t)$ is estimated from $T_f(\omega_l, b)$ by inverting the SWT [40].

$$h(t) = 2\text{Re} \left[C_\Psi^{-1} \sum_s T_f(\omega_l, b) (\Delta\omega) \right] \quad (8)$$

where $C_{\psi}^{-1} = \int_0^{+\infty} \phi^*(\varepsilon) \frac{d\varepsilon}{\varepsilon}$, $\phi^*(\varepsilon)$ is the conjugate Fourier transform of the mother wavelet, Re is the real part of the function.

3. Dispersion curves of the rail foot

3.1. Verification of the accuracy of FEM calculations

The unit cell model of an infinite steel plate with a thickness of 1 mm, length of 0.08 mm, and width of 0.08 mm is shown in Fig. 3. The maximum grid unit size of the model is 0.08 mm. The Young's modulus, Poisson's ratio, and density of the steel plate are 216.9 GPa, 0.2865, and 7932 kg/m^3 , respectively. For the x - and y -directions, the Floquet boundary conditions are used. The mesh grids in the source and target faces of the model are consistent with the replication of the meshes. The unit cell representing the periodic waveguide will extend infinitely in the x - and y -directions. Domain constraints are also used in the model to restrict the displacement in the y - and z -directions; thus, only the vibration in the x -direction is allowed. The dispersion curves of the SH-guided waves are obtained considering that the SH-guided waves are propagating in the y -direction.

The maximum values of the wavenumber k in the x - and y -directions are π/l_x and π/l_y (l_x and l_y are the lengths of the unit cell model along the x - and y -directions) [21], respectively. The eigenfrequency f corresponding to each k is solved by an eigenfrequency solver. The phase velocity c_p and group velocity c_g of the SH-guided waves can be calculated as follows [41].

$$\begin{cases} c_p = \frac{2\pi f}{k} \\ c_g = \frac{d(2\pi f)}{dk} \end{cases} \quad (9)$$

Fig. 4 shows the dispersion curves of the SH-guided waves in an infinite plate with a thickness of 1 mm. As shown in Fig. 4, the curves calculated using the FEM and Disperse software are consistent; thus, the accuracy of the FEM for solving the dispersion curves of SH-like guided waves in the rail foot is confirmed.

3.2. Dispersion curves of the SH-like guided waves in the rail foot

According to Refs. [17,18], the rail contains modes with local vibration, and the vibration of the rail head, web, and foot are independent. Coccia et al. [42] used a rail head model to calculate the dispersion curves of propagative waves of the rail head. Ramatlo et al. [43] calculated the dispersion curves of the rail web, and they used an ultrasonic piezoelectric transducer to excites a guided wave mode traveling in the rail web. Wu et al. [44] calculated the dispersion curves of propagative waves in the switch rail foot using SAFEM. According to the

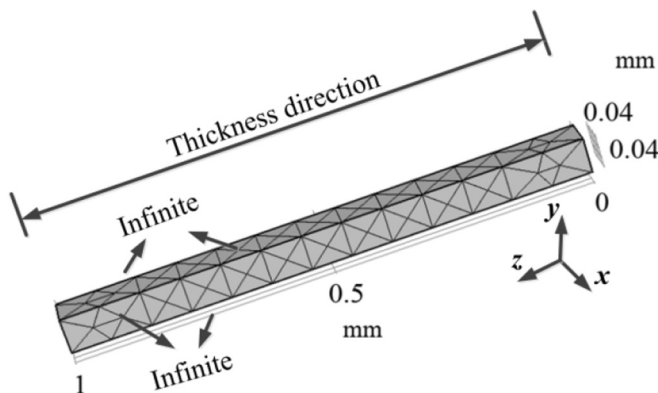


Fig. 3. Finite element model of a steel plate unit cell.

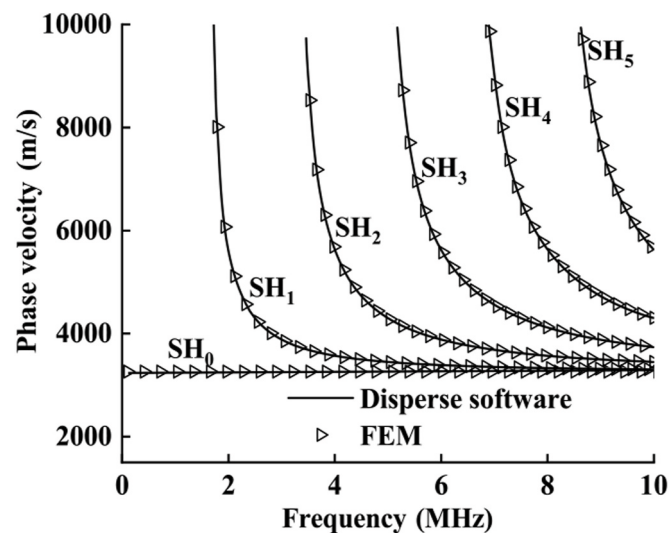


Fig. 4. Comparison between the curves calculated using the FEM and Disperse software for an infinite plate with a thickness of 1 mm.

above Refs. [17,18,42–44], a finite element model only with the rail foot is developed, and the intensity of the propagating guided wave mode is concentrated in the rail foot. Fig. 5 shows the finite element model for calculating the dispersion curves of the rail foot, and the cross-sectional dimensions of a real rail are considered according to the geometry of U60 rail. The Floquet boundary condition was used in the x -direction of the model, and the unit cell model extended infinitely in the x -direction.

Fig. 6 shows the dispersion curves of guided waves in the rail foot without the domain constraint, and the calculated dispersion curves are coincident with the curves provided Ref. [44]. As can be observed in Fig. 6, the dispersion curves contain a large number of modes in the given frequency range, and it is difficult to select the SH-like guided wave modes. Solving all the guided wave modes costs more computational time, and with the help of domain constraints, the efficiency of the solution can be improved.

Domain constraints were used to limit the displacement in the x - and y -directions; thus, only the vibration in the z -direction was allowed. Accordingly, the dispersion curves of the SH-like guided waves in the rail foot were solved. Fig. 7 shows the dispersion curves of the SH-like waves in the rail foot. The phase velocity of the guided wave mode 0 is 3177 m/s, which is the theoretical velocity of the shear wave in the rail. The SH₀ mode can propagate at all frequency values. Higher-order modes such as SH₁ and SH₂ only exist after a specific frequency value. This value above which a wave mode exists is called the cut-off point of that wave mode [45]. As shown in Fig. 7, the cut-off frequencies of the guided wave mode 1 and mode 2 are 25 kHz and 36 kHz, respectively.

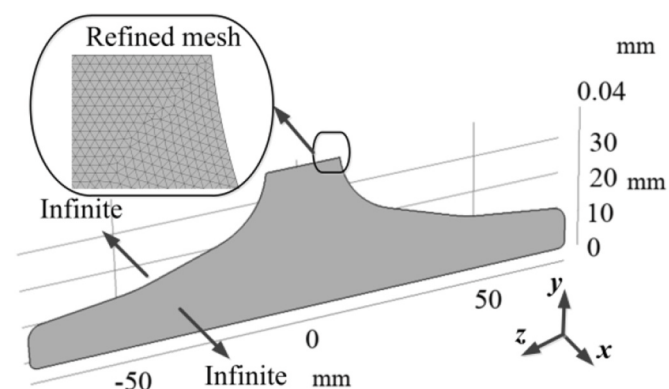


Fig. 5. Finite element model of the unit cell of rail foot.

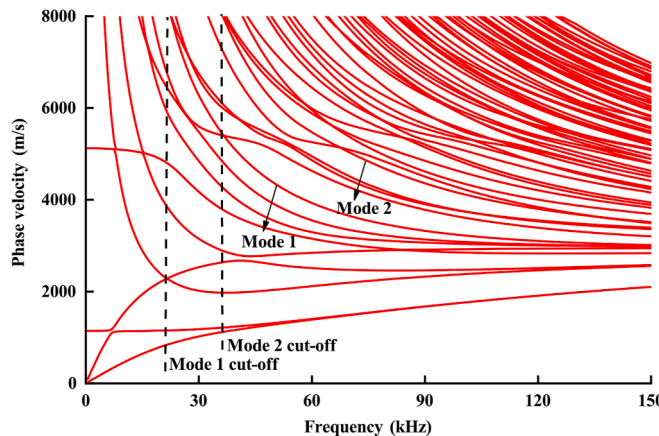


Fig. 6. Dispersion curves of the rail foot.

According to the cut-off frequencies of mode 1 and mode 2, the two modes in Fig. 6 are found, and it is can be proved that domain constraint can effectively select the SH-like guided wave modes.

When the frequency is higher than 200 kHz, the group velocities of the guided wave modes 0, 1, and 2 are almost the same; thus, the separation of these guided wave modes is difficult in the time domain. When the PPM-EMAT is used to excite the SH-like guided waves in the rail foot, the suitable frequency range is 60–200 kHz. The lower the frequency, the purer the guided wave modes. The wavelength of the guided waves increases with a decrease in frequency, and the dimensions of the magnets and the PPM-EMAT probe will be enlarged; therefore, the probe cannot perfectly fit the rail foot surface. Considering the abovementioned reasons, a PPM-EMAT probe with a permanent magnet width of 10 mm is developed, and its excitation frequency was 154 kHz.

4. Guided wave EMAT detection of the rail foot

4.1. Experimental system for guided wave EMAT detection

Fig. 8 shows the experimental arrangement of the guided wave EMAT used for the detection of cracks in the rail foot. A straight crack with a length of 15 mm, width of 1 mm, and depth of 14 mm was produced in the rail foot. A tone-burst signal is generated by a signal generator (Agilent 33220A) and then amplified by the power amplifier (RITEC GA-2500A). An impedance matching network is used between

the power generator and the EMAT coil, and the power transmitted from the power generator to the EMAT can be maximized. Under Lorentz forces and magnetostriction effect, the SH-guided waves are excited in the rail foot, and they propagate along the length direction of the rail. When the SH-guided waves are received by the EMAT receiver, the ultrasonic signal is maximized by the impedance matching network, and the amplitude of the signal is amplified by a preamplifier (OLYMPUS 5072 PR). The amplified signal is collected by the data acquisition card (ART Technology NET8544), which is then connected to the personal computer for signal analysis and processing.

The excitation and reception EMATs have a racetrack coil with a conductor diameter of 0.35 mm, and the length and width of the race-track coil are 110 mm and 50 mm, respectively. The PPM-EMAT probe has six pairs of permanent magnets, and the length, width and height of the permanent magnet are 20 mm, 10 mm, and 10 mm respectively.

4.2. Application of the SWT in the guided wave EMAT detection with a high lift-off

There may be local corrosion or surface attachments on the rail foot that has been in use for a long time; hence, we should increase the lift-off of the EMAT to meet the irregularities of the rail foot surface. However, the SNR of the ultrasonic echo sharply dropped with an increase in the lift-off of the EMAT. Therefore, some signal processing methods should be explored for the detection of cracks in the rail foot using an EMAT with a large lift-off and strong noises. SNR is defined here as [46].

$$\text{SNR} = 20\lg(V_s / V_n) \quad (10)$$

where V_s is the maximum amplitude of the signal and V_n is the noise level which is taken as the root mean square of the whole signal.

The excitation and sampling frequencies of the EMAT detection system are 0.154 MHz and 40 MHz, respectively. The transmitter is excited by a tone-burst pulse for five cycles, and the ultrasonic echoes are processed by 64 synchronous averages. Fig. 9 shows the ultrasonic signal detected at different EMAT lift-offs. With an increase in the lift-off, the amplitude of the echo signals rapidly dropped (Fig. 9). When the lift-off was 4 mm, the defective signal was buried in the noise, and the defect echo could not be effectively identified.

The echo signal with a lift-off of 4 mm was processed by the SWT, and the time-frequency diagram is shown in Fig. 10. As can be observed in Fig. 10, the main frequency component of the original signal is approximately 0.154 MHz, and the dotted noises are in the high-frequency zone. After squeezing the time-frequency spectrum to the center frequency, the energy is focussed on the time and frequency directions. The time-frequency resolution significantly improved, and the

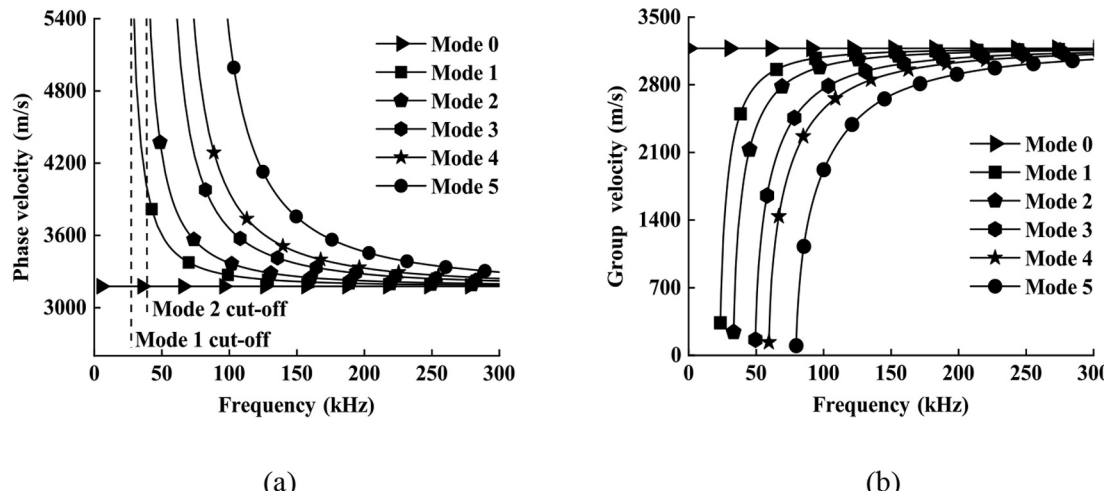


Fig. 7. Dispersion curves of the SH-like guided waves in the rail foot: (a) phase velocity and (b) group velocity.

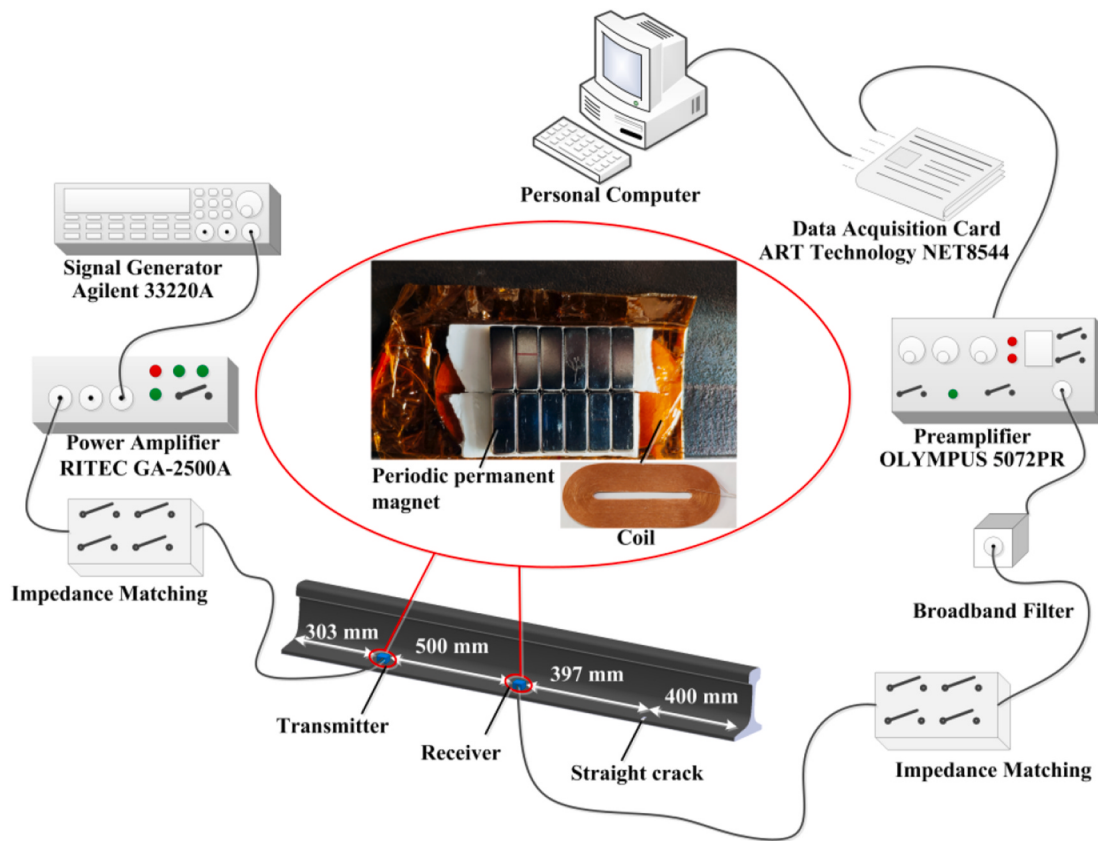


Fig. 8. The EMAT detection system for the rail foot.

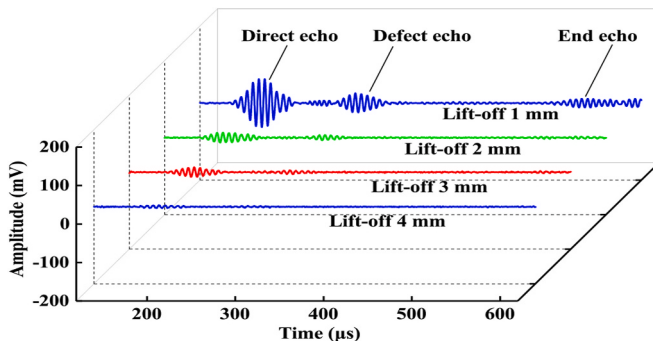


Fig. 9. Comparison between the A-scan waveforms obtained at different EMAT lift-offs.

defect echo was separated from the noises. The time–frequency diagram was divided and analyzed, and the SH-like guided wave $T_f(\omega_l, b)$ in the frequency direction could be extracted. The SH-like guided wave signal was reconstructed using Equation (8), and the reconstructed signal is shown in Fig. 11. As can be noticed in Fig. 11, the SNR of the reconstructed signal is greatly improved when compared with that of the original signal.

The original signals obtained at different lift-offs were processed by the SWT, and the SNRs of the original and reconstructed signals were calculated (Fig. 12). As observed in Fig. 12, the SNR of the SWT-processed signal was significantly improved. When the EMAT lift-off was 1 mm, the SNR of the ultrasonic signal was increased by 5.98 dB after SWT processing. When the EMAT lift-off was 4 mm, the SNR of the ultrasonic signal was increased by 16.63 dB after SWT processing.

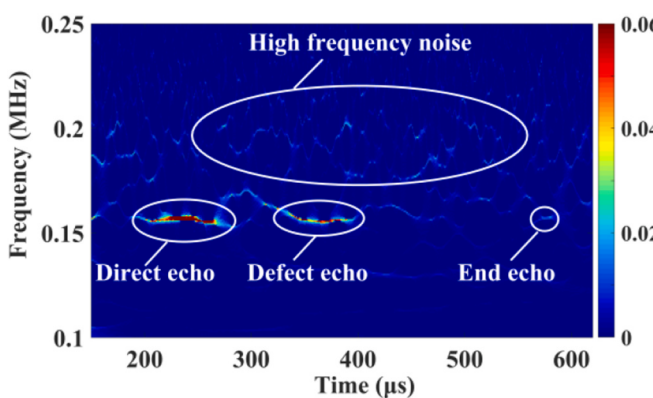


Fig. 10. SWT time–frequency diagram.

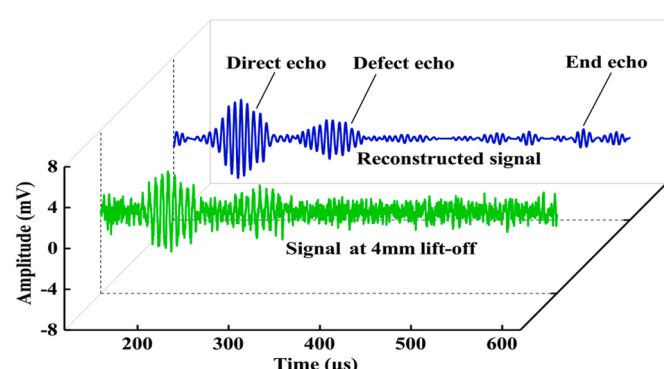


Fig. 11. Comparison between the signals obtained at 4 mm lift-off before and after SWT processing.

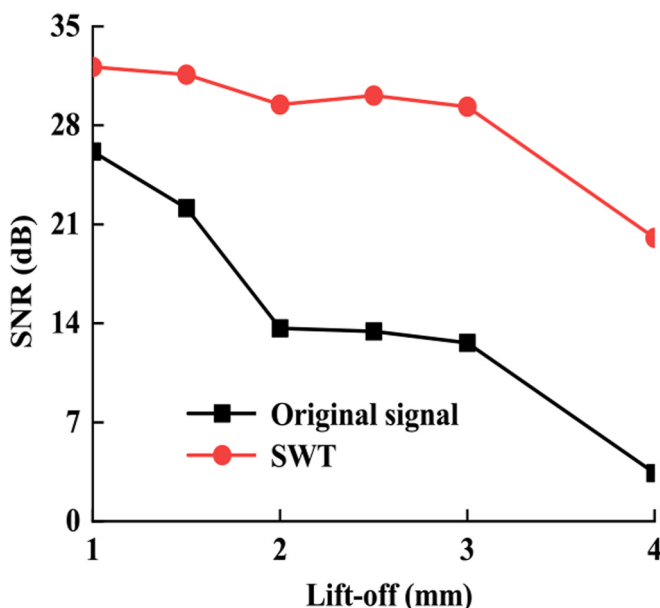


Fig. 12. Comparison between the SNRs of the signals obtained before and after SWT processing.

4.3. Application of SWT in the single-mode extraction of guided waves

When a guided wave propagates in the wedge-shaped rail foot, multiple guided wave modes are easily generated. To verify the function of the SWT in mode separation, it is necessary to excite the guided wave signal contain higher- and low-order with the same intensity. Excitation current with multiple cycles will minimize the dispersion effect, so a tone-burst pulse with one cycle was used to excite the EMAT. As the amplitude of the ultrasonic signal is in a sharp decrease as the duration of the tone-burst pulse is reduced when the duration is less than a certain value, so it is hard to increase the EMAT's lift-off. When a tone-burst pulse with one cycle is used as the excitation signal and the lift-offs of the two EMAT are 0.1 mm, an ultrasonic signal with 64 synchronous averages is obtained, and it is shown in Fig. 13(a). As can be noticed in Fig. 13(a), the wave packets of the signal are aliasing, and only the direct echo can be identified. The original signal was processed by the SWT, and the time-frequency diagram is shown in Fig. 14. According to Fig. 14, the original signal was divided into two parts: low- and higher-order SH-like guided wave modes. Fig. 13(b) and (c) show the signals of the low- and higher-order SH-like guided wave modes after reconstruction. According to Fig. 13(b) and (c), via the reconstructed signals of the low- and higher-order SH-like guided wave modes, the defect echoes can be effectively identified.

4.4. Ultrasonic B-scan imaging of straight cracks in the rail foot

It is difficult to excite a single guided wave mode in the rail foot, and the low- and higher-order guided wave modes simultaneously propagate in the rail foot. To achieve effective detection of cracks in the rail foot, it is necessary to remove the higher-order guided wave modes. The lift-offs of the two EMATs were 0.1 mm, and these EMATs were excited with a tone-burst pulse for five cycles.

The dispersion curves of the group velocity of the rail foot were transformed into the time-frequency domain through coordinate transformation, and the direct echo mode was identified, as shown in Fig. 15. As can be observed in Fig. 15, the excited SH-like guided waves are mainly in mode 0, and there are higher-order modes such as modes 1, 2, and 3. Due to the large attenuation of higher-order modes, these modes gradually disappear. However, the higher-order modes still affect the effective identification of the defect echoes. Fig. 16 shows the

original and reconstructed signals. As depicted in Fig. 16, the higher-order modes were successfully removed by SWT processing.

Ultrasonic B-scan images were obtained under the following conditions: the distance from the left end of the rail to the transmitter was 303 mm; the distance between the transmitter and the receiver was fixed at 500 mm; the distance from the receiver to the straight crack was 397 mm; and the distance from the straight crack to the right end of the rail was 400 mm. The excitation and reception EMATs were moved towards the crack, and the ultrasonic echo signals were obtained. Herein 81 detection points with a scanning step of 3 mm were scanned; at each point, 64 groups of signals were acquired for synchronous averaging.

Fig. 17 shows the ultrasonic B-scan image with 81 groups of detected signals without the SWT processing. The defect echo and the end echo can be directly identified; however, there is a higher-order mode between the direct echo and the defect echo (Fig. 17). Fig. 18 shows the ultrasonic B-scan image with 81 groups of detected signals after the SWT processing. According to Fig. 18, higher-order modes were effectively removed by the SWT processing. The quality of the ultrasonic B-scan image was improved, and the position and depth of the crack were better highlighted.

4.5. Application of SWT in rapid crack detection

Synchronous averaging is an effective method for improving the SNR of the detected ultrasonic signal; however, the detection time increases with an increase in the number of synchronous averages; this limits the rapid detection of cracks in railroad lines. To achieve rapid detection of cracks in the rail foot, an ultrasonic signal with a relatively high SNR but with no synchronous average is required. When a tone-burst pulse with five cycles is used and the lift-offs of the two EMAT are 0.1 mm. The SNR of the ultrasonic signal with no synchronous average was 10.57 dB, and the SNR of the reconstructed signal was 28.36 dB; thus, the SNR of this signal was improved by 17.79 dB after the SWT processing (Fig. 19). As shown in Fig. 19, the SNR of the reconstructed signal is higher than that of the signal with 64 synchronous averages, and it was improved by 5.42 dB.

The 81 groups of signals with no synchronous average were imaged by ultrasonic B-scan imaging, and the imaging result is shown in Fig. 20. As depicted in Fig. 20, there are too many background noises in the image, and the ridgeline of the crack can be observed in the image; however, the accurate position of the crack cannot be detected. Fig. 21 shows the ultrasonic B-scan image reconstructed by the SWT. As can be observed in Fig. 21, the reconstructed image clearly shows the position of the crack in the rail foot. Furthermore, the background noise and higher-order modes were successfully removed by the SWT processing.

When the pulse repetition rate of the pulse power amplifier for the generating EMAT is 20 Hz and the 64 synchronous averaging is used, the spent time is 3.2 s. But for the raw ultrasonic wave signal without synchronous averaging and processed by SWT, the spent time is 0.05 s. Besides, the SNR of the reconstructed signal is higher than that of the signal with 64 synchronous averages, and the SNR of the former can be improved by 5.42 dB. With the application of SWT, the SNR of the received ultrasonic wave signal can be enhanced without increasing the number of synchronous averaging. In this way, the detection speed can be improved which is a special need for the rail-line inspection.

4.6. Application of SWT in rapid crack detection with large lift-off

When a tone-burst pulse with five cycles was used as the excitation signal and the lift-off of the two EMATs are 4 mm. 81 groups of ultrasonic signals with no synchronous average were imaged by ultrasonic B-scan imaging, and the imaging result is shown in Fig. 22. As depicted in Fig. 22, the ridgeline of the crack is buried in the noise, and the position of the crack cannot be effectively identified. Fig. 23 shows the ultrasonic B-scan image reconstructed by the SWT. As can be observed in Fig. 23, the defect echo and the end echo can be directly identified in the image

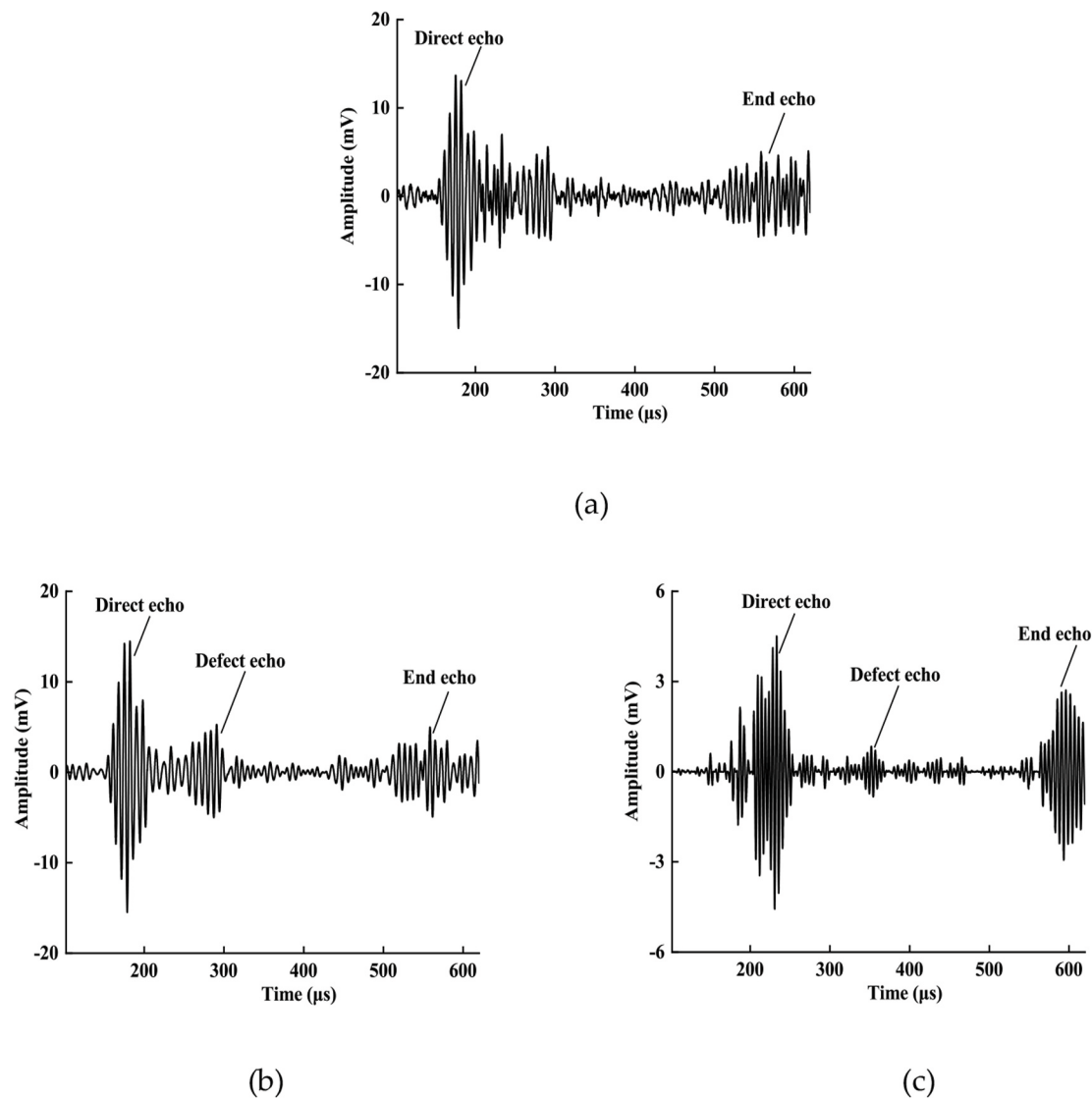


Fig. 13. SWT reconstructed signals of the low- and higher-order SH-like guided wave modes: (a) original signal and signals of the (b) low- and (c) higher-order SH-like guide wave modes.

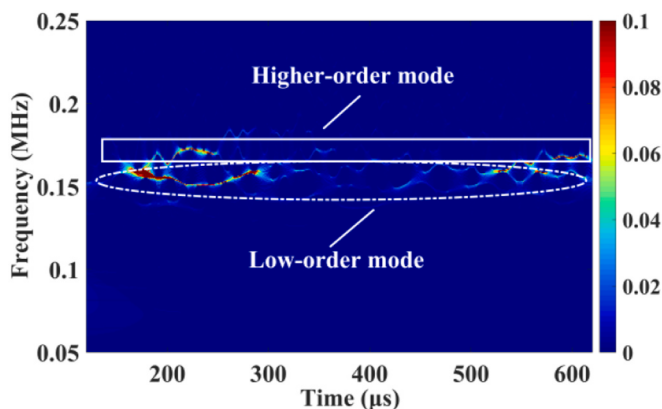


Fig. 14. Time–frequency diagram of the original ultrasonic signal.

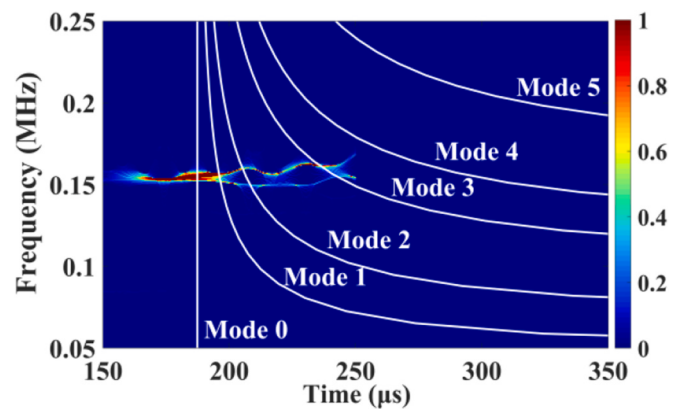


Fig. 15. Identification of the direct ultrasonic echo modes by time–frequency analysis.

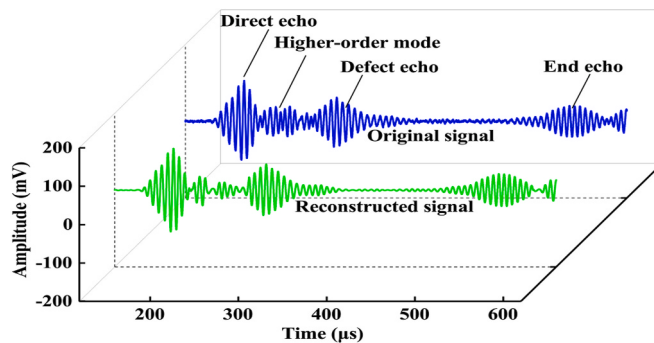


Fig. 16. Comparison between the ultrasonic signals obtained before and after the SWT processing.

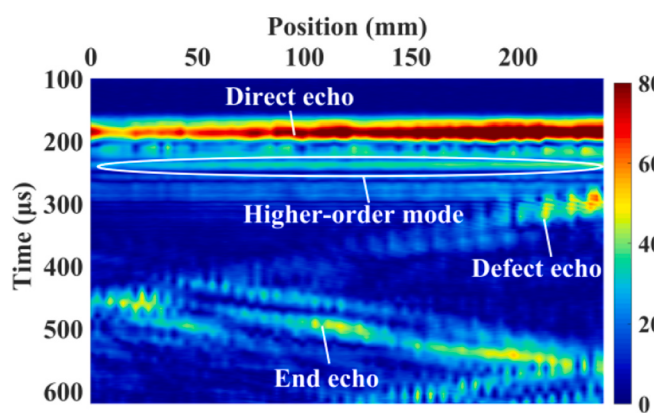


Fig. 17. Ultrasonic B-scan image without the SWT processing.

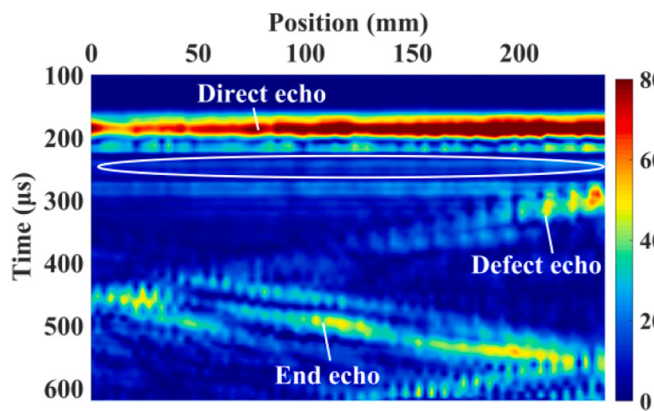


Fig. 18. Ultrasonic B-scan image with the SWT processing.

with no synchronous average and a larger lift-off.

5. Conclusion

Herein, an ultrasonic B-scan imaging-based SH-guided wave EMAT is proposed for the rapid detection of cracks in the rail foot. The proposed solution method of dispersion curves and reconstruction method of guided wave modes have been proven to be effective via experimental investigations. This method mainly enables the guided wave detection of structures, including the rail foot, with wedge-shaped waveguide characteristics, such as the rapid detection of the rail foot. The main conclusions of this study are as follows:

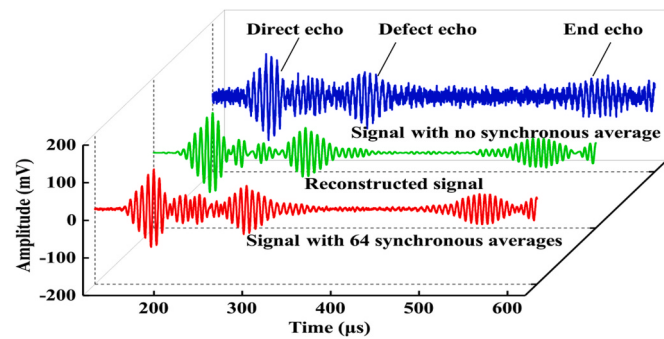


Fig. 19. Ultrasonic signals with the synchronous averages and SWT processing.

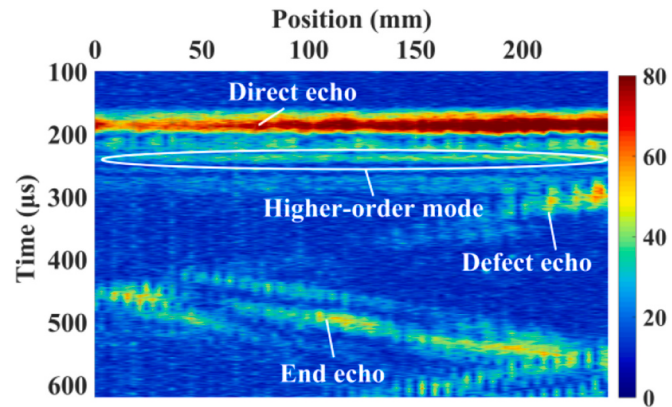


Fig. 20. Ultrasonic B-scan image with no synchronous average and no SWT processing.

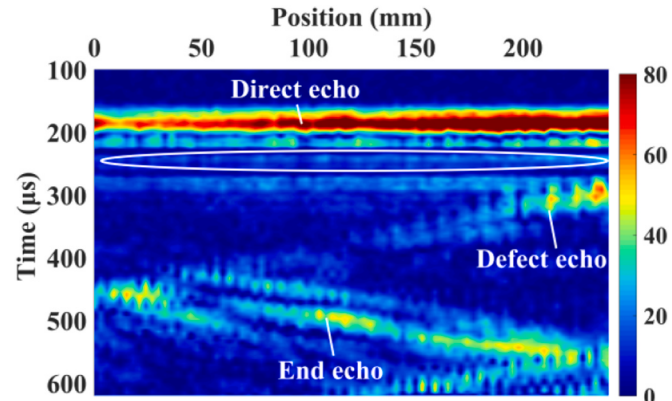


Fig. 21. Ultrasonic B-scan image reconstructed by the SWT without a synchronous average.

- (1) Based on the Bloch–Floquet theory and FEM, the dispersion curves of SH-like guided waves in the rail foot can be solved. This method can be used to compute the dispersion curves of SH-like guided waves in periodic waveguides with arbitrary cross-sections.
- (2) The lift-off of the EMAT has a significant influence on the SNR of the echo signal. The SWT can effectively eliminate the strong noises in the signals. When the EMAT lift-off was 4 mm, the SNR of the original ultrasonic signal could be increased by 16.63 dB via SWT processing. This signal processing provides a new method for the detection of cracks in the rail foot by the SH-like guided wave EMAT with a large lift-off.

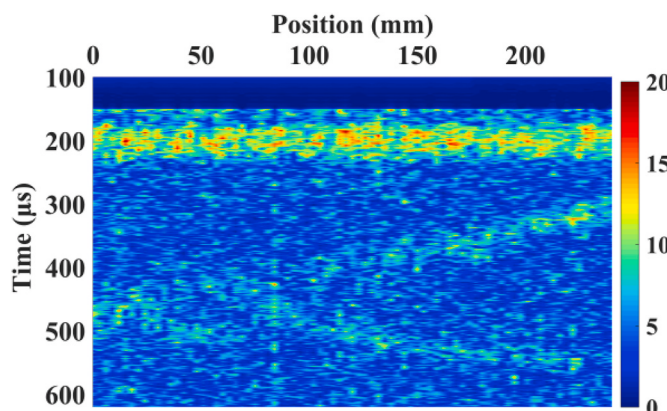


Fig. 22. Ultrasonic B-scan image with no synchronous average and no SWT processing when EMAT lift-off is 4 mm.

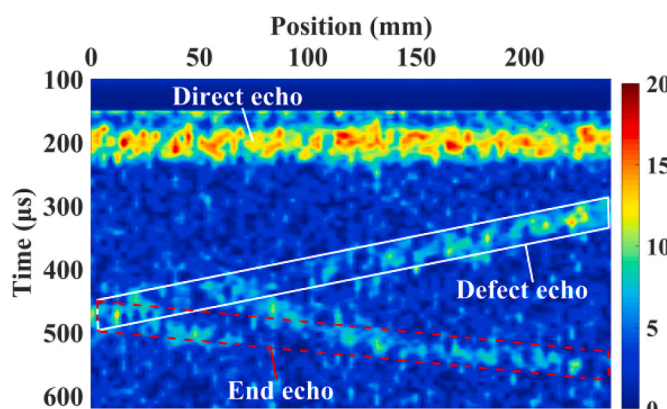


Fig. 23. Ultrasonic B-scan image reconstructed by the SWT without a synchronous average when EMAT lift-off is 4 mm.

- (3) The cracks in the rail foot can be effectively detected by ultrasonic B-scan imaging using a guided wave EMAT. The SWT can effectively remove higher-order guided wave modes. The quality of the ultrasonic B-scan image was improved after the reconstruction of the detected signals by SWT, which provides a new method for the single-mode guided wave detection of cracks in the rail foot.
- (4) The ultrasonic signal with no synchronous average exhibits a higher SNR after the SWT processing than that of the signal with 64 synchronous averages; thus, the SWT processing substantially reduces the detection time. This study provides a new method for the rapid detection of cracks in the rail foot by ultrasonic B-scan imaging.

Funding

This work was supported by the National Natural Science Foundation of China (grant numbers: 12064001, 52065049 and 51705231), Jiangxi Provincial Natural Science Foundation (grant numbers: 20192ACBL20052), Opening Foundation of National Key Laboratory of Sound Field and Sound Information (grant number: SKLA201912).

Declaration of competing interest

The authors declare that they have no known competing financial interests or personal relationships that could have appeared to influence the work reported in this paper.

References

- [1] Clark R. Rail flaw detection: overview and needs for future developments. *NDT&E Int* 2004;37(2):111–8.
- [2] Loveday PW, Long CS, Ramatlo DA. Ultrasonic guided wave monitoring of an operational rail track. *Struct Health Monit* 2019;19(6):1666–84.
- [3] Rose JL. A baseline and vision of ultrasonic guided wave inspection potential. *J Press Vess-T Asme* 2002;124(3):273–82.
- [4] Rose JL, Avioli MJ, Mudge P, Sanderson R. Guided wave inspection potential of defects in rail. *NDT&E Int* 2004;37(2):153–61.
- [5] Edwards RS, Sophian A, Dixon S, Tian GY, Jian X. Dual EMAT and PEC non-contact probe: applications to defect testing. *NDT&E Int* 2006;39(1):45–52.
- [6] Petcher PA, Potter MDG, Dixon S. A new electromagnetic acoustic transducer (EMAT) design for operation on rail. *NDT&E Int* 2014;65:1–7.
- [7] Nakamura N, Ashida K, Takishita T, Ogi H, Hirao M. Inspection of stress corrosion cracking in welded stainless steel pipe using point-focusing electromagnetic-acoustic transducer. *NDT&E Int* 2016;83:88–93.
- [8] Li J, Rose JL. Natural beam focusing of non-axisymmetric guided waves in large-diameter pipes. *Ultrasonics* 2006;44(1):35–45.
- [9] Sun H, Peng L, Huang S, Wang Q, Wang S, Zhao W. Analytical model and optimal focal position selection for oblique point-focusing shear horizontal guided wave EMAT. *Construct Build Mater* 2020;258:120375.
- [10] Lee JS, Kim YY, Cho SH. Beam-focused shear-horizontal wave generation in a plate by a circular magnetostrictive patch transducer employing a planar solenoid array. *Smart Mater Struct* 2009;18(1):015009.
- [11] Thring CB, Fan Y, Edwards RS. Multi-coil focused EMAT for characterisation of surface-breaking defects of arbitrary orientation. *NDT&E Int* 2017;88:1–7.
- [12] Coccia S, Bartoli I, Marzani A, Scalea FLD, Salamone S, Fateh M. Numerical and experimental study of guided waves for detection of defects in the rail head. *NDT&E Int* 2011;44(1):93–100.
- [13] Hesse D, Cawley P. Surface wave modes in rails. *J Acoust Soc Am* 2006;120(2):733–40.
- [14] Chen F, Wilcox PD. The effect of load on guided wave propagation. *Ultrasonics* 2007;47(1–4):111–22.
- [15] Gavrić L. Computation of propagative waves in free rail using a finite element technique. *J Sound Vib* 1995;185(3):531–43.
- [16] Hayashi T, Song WJ, Rose JL. Guided wave dispersion curves for a bar with an arbitrary cross-section, a rod and rail example. *Ultrasonics* 2003;41(3):175–83.
- [17] Hayashi T, Miyazaki Y, Murase M, Abe T. Guided wave inspection for bottom edge of rails. *AIP Conf Proc* 2007;894:169–76.
- [18] Hayashi T, Tamayama C, Murase M. Wave structure analysis of guided waves in a bar with an arbitrary cross-section. *Ultrasonics* 2006;44(1):17–24.
- [19] Treyyssède F. Numerical investigation of elastic modes of propagation in helical waveguides. *J Acoust Soc Am* 2007;121(6):3398–408.
- [20] Treyyssède F. Elastic waves in helical waveguides. *Wave Motion* 2008;45(4):457–70.
- [21] Hakoda C, Rose JL, Shokouhi P, Lissenden C. Using Floquet periodicity to easily calculate dispersion curves and wave structures of homogeneous waveguides. 16–21 July 1949. Provo, Utah, USA. In: 44th Annual Review of Progress in Quantitative Nondestructive Evaluation (QNDE); 2017. 020016-1–020016-10. <https://doi.org/10.1063/1.5031513>.
- [22] Daubechies I, Lu J, Wu HT. Synchrosqueezed wavelet transforms: an empirical mode decomposition-like tool. *Appl Comput Harmon Anal* 2011;30(2):243–61.
- [23] Herrera RH, Han J, Baan MVD. Applications of the synchrosqueezing transform in seismic time-frequency analysis. *Geophysics* 2014;79(3):V55–64.
- [24] Thakur G, Brevoort E, Fučík NS, Wu HT. The Synchrosqueezing algorithm for time-varying spectral analysis: robustness properties and new paleoclimate applications. *Signal Process* 2013;93(5):1079–94.
- [25] Amezcua-Sánchez JP, Adeli H. Synchrosqueezed wavelet transform-fractality model for locating, detecting, and quantifying damage in smart highrise building structures. *Smart Mater Struct* 2015;24(6):065034.
- [26] Wu HT, Chan YH, Lin YT, Yeh YH. Using synchrosqueezing transform to discover breathing dynamics from ECG signals. *Appl Comput Harmon Anal* 2014;36(2):354–9.
- [27] Su C, Jiang M, Liang J, Tian A, Sun L, Zhang L, et al. Damage assessments of composite under the environment with strong noise based on synchrosqueezing wavelet transform and stack autoencoder algorithm. *Measurement* 2020;156:107587.
- [28] Bause F, Huang B, Kunoth A, Henning B. Ultrasonic waveguide signal decomposition using the synchrosqueezed wavelet transform for modal group delay computation. Prague, Czech Republic. In: 2013 IEEE International Ultrasonics Symposium (IUS); 2013. p. 671–4. 21–25 July 2013, <https://doi.org/10.1109/ULTSYM.2013.0173>.
- [29] Liu Z, Xu K, Li D, Ta D, Wang W. Automatic mode extraction of ultrasonic guided waves using synchrosqueezed wavelet transform. *Ultrasonics* 2019;99:105948.
- [30] Moser F, Jacobs LJ, Qu J. Modeling elastic wave propagation in waveguides with the finite element method. *NDT&E Int* 1999;32(4):225–34.
- [31] Lidström P, Olsson P. On the natural vibrations of linear structures with constraints. *J Sound Vib* 2007;301(1):341–54.
- [32] Axmann W, Kuchment P. An efficient finite element method for computing spectra of photonic and acoustic band-gap materials. *J Comput Phys* 1999;150(2):468–81.
- [33] Ribichini R, Cegla F, Nagy PB, Cawley P. Study and comparison of different EMAT configurations for SH wave inspection. *IEEE T Ultrason Ferr* 2011;58(12):2571–81.
- [34] Ribichini R, Nagy PB, Ogi H. The impact of magnetostriction on the transduction of normal bias field EMATs. *NDT&E Int* 2012;51:8–15.

- [35] Petcher PA, Dixon S. Weld defect detection using PPM EMAT generated shear horizontal ultrasound. *NDT&E Int* 2015;74:58–65.
- [36] Ribichini R, Cegla F, Nagy PB, Cawley P. Experimental and numerical evaluation of electromagnetic acoustic transducer performance on steel materials. *NDT&E Int* 2012;45(1):32–8.
- [37] Sun H, Huang S, Wang Q, Wang S, Zhao W. Improvement of unidirectional focusing periodic permanent magnet shear-horizontal wave electromagnetic acoustic transducer by oblique bias magnetic field. *Sensor Actuat A Phys* 2019;290:36–47.
- [38] Feng B, Ribeiro AL, Ramos HG. A new method to detect delamination in composites using chirp-excited Lamb wave and wavelet analysis. *NDT&E Int* 2018; 100:64–73.
- [39] Liu Z, Lin B, Liang X, Du A. Time-frequency analysis of laser-excited surface acoustic waves based on synchrosqueezing transform. *Ultrasonics* 2020;106: 106147.
- [40] Jiang Q, Suter BW. Instantaneous frequency estimation based on synchrosqueezing wavelet transform. *Signal Process* 2017;138:167–81.
- [41] Loveday PW, Long CS, Ramatlo DA. Mode repulsion of ultrasonic guided waves in rails. *Ultrasonics* 2018;84:341–9.
- [42] Coccia S, Bartoli I, Marzani A, Scalea FL, Salamone S, Fateh M. Numerical and experimental study of guided waves for detection of defects in the rail head. *NDT&E Int* 2011;44(1):93–100.
- [43] Ramatlo DA, Wilke DN, Loveday PW. Development of an optimal piezoelectric transducer to excite guided waves in a rail web. *NDT&E Int* 2018;95:72–81.
- [44] Wu J, Tang Z, Lü F, Yang K. Ultrasonic guided wave focusing in waveguides with constant irregular cross-sections. *Ultrasonics* 2018;89:1–12.
- [45] Suresh N, Balasubramaniam K. Quantifying the lowest remnant thickness using a novel broadband wavelength and frequency EMAT utilizing the cut-off property of guided waves. *NDT&E Int* 2020;116:102313.
- [46] Pedram SK, Fateri S, Gan L, Haig A, Thorncroft K. Split-spectrum processing technique for SNR enhancement of ultrasonic guided wave. *Ultrasonics* 2018;83: 48–59.